ChemComm

COMMUNICATION

View Article Online
View Journal | View Issue

Cite this: *Chem. Commun.*, 2025, 61, 19917

Received 11th October 2025,
Accepted 19th November 2025

DOI: 10.1039/d5cc05797c

rsc.li/chemcomm

Coupling of manganese oxidative crystallization and thallium immobilization under light irradiation

Jielong Cao,[abcd] Qingze Chen,[*abcd] Xun Liu,[abcd] Yixuan Yang,[abc] Hongbo Li,[abc] Juan Liu[e] and Runliang Zhu[abcd]

This study investigates the mutual influence of Mn(II) oxidative crystallization and thallium (Tl) immobilization in nitrate solution under light irradiation. MnO_x formed by the photochemical oxidation of Mn(II) effectively removed Tl(I) through adsorption and coprecipitation, with Mn(II) inhibiting the oxidation of Tl(I) to more toxic Tl(III). In turn, Tl(I) suppressed the reductive transformation of δ-MnO_2, which favored its own immobilization.

Manganese (oxyhydr)oxides (MnO_x) are ubiquitously distributed across various geological settings, including marine, soil, and sediment.[1] Due to their relatively high specific surface area and high redox and adsorption reactivity, MnO_x exert strong control over the geochemical processes on the Earth's surface, such as the redox cycling, as well as the migration and transformation of environmental substances.[2] The reactivity of MnO_x is intrinsically governed by their crystalline structure and valence state composition, making the understanding of their formation and transformation processes fundamentally essential.

Soluble Mn(II) ions are readily oxidized to MnO_x through biotic and abiotic processes. Microbially mediated Mn(II) oxidation is recognized as the predominant pathway for natural MnO_x formation, owing to its rapid oxidation kinetics (several orders of magnitude faster than abiotic processes).[3,4] However, emerging research has revealed that photochemically produced reactive intermediates generated from various environmental components (*e.g.*, nitrate,[5] natural semiconductor minerals,[6] nanoplastics,[7] and dissolved organic matter[8]) can oxidize Mn(II) at rates comparable to those of currently known biotic and abiotic oxidation processes. This finding indicates that the photochemical oxidation of Mn(II) plays a vital role in the formation of MnO_x in natural systems.

As important natural metal scavengers, MnO_x can effectively immobilize various metal ions through multiple mechanisms, including adsorption, oxidation, ion exchange, and surface-induced precipitation.[9,10] One example is thallium (Tl), a highly toxic but underestimated heavy metal.[11,12] Due to abundant natural (*e.g.*, weathering of Tl-bearing rocks/minerals) and anthropogenic (*e.g.*, mining, smelting, and coal combustion) sources, Tl is widely distributed in water, soil, sediment, and the atmosphere.[13,14] Monovalent Tl(I) primarily exists as free cations, while trivalent Tl(III) is readily hydrolyzed to form avicennite.[15] The formation and transformation of MnO_x play crucial roles in the biogeochemical cycling of Tl due to the high geochemical affinity and strong correlation between MnO_x and Tl.[16,17] For example, Tl(I) is effectively removed during biogenic Mn(II) oxidation, with 64% of Tl(I) being oxidized to Tl(III).[18] Furthermore, anoxic MnO_2 transformation driven by Mn(II)/Fe(II) can enhance Tl mobilization.[19] However, the coupled cycling of Mn and Tl under light irradiation in the Earth's surface environments remains poorly elucidated.

Herein, we focus on an important natural abiotic Mn–Tl process for the first time and reveal the details about the coupling between the Mn redox cycle and Tl immobilization under irradiation. The proposed light-driven Mn redox cycle is composed of three key processes: (i) the oxidation of Mn(II) to δ-MnO_2 by superoxide radicals ($O_2^{\bullet-}$) generated from the photolysis of nitrate; (ii) the reductive transformation of δ-MnO_2 *via* Mn(II) + Mn(IV) ⇌ 2Mn(III); and (iii) the photoreduction of the formed MnO_x and reoxidation of Mn(II). The formed MnO_x effectively removed Tl(I) through adsorption and coprecipitation, with Mn(II) inhibiting Tl(I) oxidation. In turn, Tl(I) suppressed the reductive transformation of δ-MnO_2 due to the competition between Mn(II) and Tl(I). Our results enhance the comprehension of the coupled environmental geochemical processes involving Mn and Tl in natural systems and offer new insights for environmental remediation.

[a] *State Key Laboratory of Advanced Environmental Technology, Guangzhou Institute of Geochemistry, Chinese Academy of Sciences, Guangzhou 510640, China. E-mail: chenqingze@gig.ac.cn*
[b] *Guangdong Provincial Key Laboratory of Mineral Physics and Materials, Guangzhou Institute of Geochemistry, Chinese Academy of Sciences, Guangzhou 510640, China*
[c] *Guangdong Research Center for Strategic Metals and Green Utilization, Guangzhou 510640, China*
[d] *University of Chinese Academy of Science, Beijing 100049, China*
[e] *School of Environmental Science and Engineering, Guangzhou University, Guangzhou 510006, China*

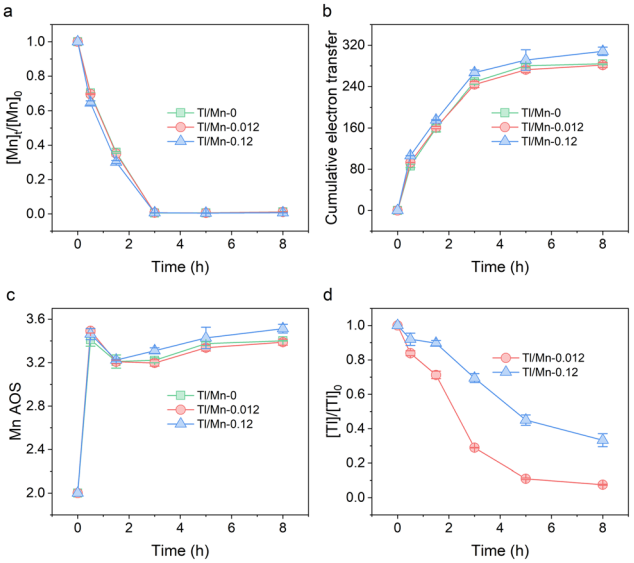

Fig. 1 Changes in (a) Mn concentration, (b) cumulative electron transfer (in units of μmol e^- L^{-1}), (c) Mn AOS, and (d) Tl concentration during the reaction.

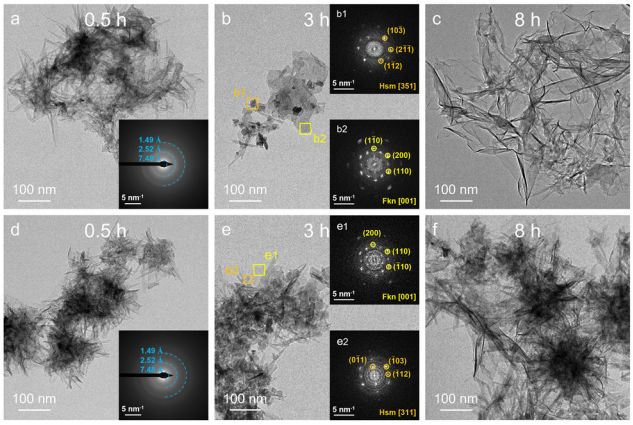

Fig. 2 Representative TEM images of the solid samples collected at different time intervals (0.5, 3, 8 h) from Tl/Mn-0 (a)–(c) and Tl/Mn-0.12 (d)–(f). The insets in panels (a) and (d) are their corresponding overall SAED patterns. Affiliated panels (b1, b2) and (e1, e2) are the FFT patterns corresponding to the selected areas in panels (b) and (e), respectively.

The photochemical experiments were conducted using 1 mM nitrate and different Tl/Mn molar ratios (0, 0.012, and 0.12) at pH 8. The cumulative electron transfer increased rapidly with the decrease of Mn concentration during the reaction (Fig. 1a and b), indicating the rapid oxidation of Mn(II) to MnO_x. Furthermore, the rate constants of Mn(II) oxidation increased with the increase in the Tl/Mn molar ratio (Table S1, SI). The concentration of Tl progressively decreased coupled with MnO_x formation, achieving removal efficiencies of 92.48% and 66.71% after 8 h for Tl/Mn-0.012 and Tl/Mn-0.12, respectively (Fig. 1d). Interestingly, the calculated Mn average oxidation state (AOS) exhibited a distinctive "increase–decrease–increase" trend during the reaction (Fig. 1c), implying the complex redox dynamics during MnO_x formation. Hence, solid samples collected at different time intervals (0.5, 3, and 8 h) were analyzed to trace the formation pathway of MnO_x.

No diffraction peaks were observed in the XRD patterns after 0.5 h of reaction, whereas the characteristic diffraction peaks corresponding to feitknechtite, hausmannite, and δ-MnO_2 emerged as the reaction progressed (Fig. S4, SI). Transmission electron microscopy (TEM) images revealed that MnO_x at 0.5 h primarily exhibited a dendritic morphology, and the selected area electron diffraction (SAED) patterns displayed diffraction rings at 0.748 nm, 0.252 nm, and 0.149 nm (Fig. 2a and d), corresponding to the (001), (200), and (310) planes of δ-MnO_2, respectively. After 3 h of reaction, the TEM images showed plenty of plate-like and granular particles (Fig. 2b and e), which were identified as feitknechtite and hausmannite, respectively, by fast Fourier transformation (FFT) analysis of the corresponding areas (Fig. 2b1, b2, e1 and e2). Feitknechtite serves as a key metastable transformation product during the reaction between δ-MnO_2 and Mn(II), which may subsequently convert into either manganite or hausmannite.[20] Combining the decrease of Mn AOS and the evolution of MnO_x phases between 0.5 and 3 h, we proposed that the formed δ-MnO_2 was subsequently reduced by surface-adsorbed Mn(II). In addition, MnO_x of Tl/Mn-0.12 retained the morphology of δ-MnO_2 (Fig. 2e), and the proportions of Mn(IV) increased with the increase in the Tl/Mn molar ratio (Fig. S5 and Table S2, SI), which implied that Tl suppressed the reductive transformation of δ-MnO_2. The Mn AOS continued to increase between 3 and 8 h (Fig. 1c), despite the complete consumption of aqueous Mn. The morphology and average particle size of MnO_x underwent a significant change after 8 h (Fig. 2c, f and Fig. S6, SI), which could be explained by the photoreductive dissolution of MnO_x and reoxidation of Mn(II).[21] After the exclusion of oxidants (*i.e.*, nitrate and oxygen), the electron transfer amount decreased gradually under irradiation (Fig. S7, SI), confirming the photoreduction of MnO_x. Besides, we found that Tl had a negligible effect on this process (Fig. S7, SI). Above all, we proposed a Mn redox cycle under light irradiation, which comprised: (i) Mn(II) oxidation to δ-MnO_2; (ii) phase transformation of δ-MnO_2 into feitknechtite and hausmannite *via* Mn(II) + Mn(IV) $\rightleftharpoons$ 2Mn(III); and (iii) photoreduction of MnO_x and reoxidation of Mn(II).

The mechanisms for Mn(II) oxidation were explored through a series of experiments specifically aimed at uncovering the dominant pathways and key intermediates. Due to the symmetry mismatch between the molecular orbitals of $Mn(H_2O)_6^{2+}$ and O_2, the electron transfer from Mn(II) to O_2 proceeds at a very slow rate, particularly when the pH is below 8.5.[22] The negligible removal of Mn under dark conditions aligns with the above perspective (Fig. S8, SI). In a nitrate-free system, the concentration of Mn decreased by 17.17% within 8 h (Fig. 3a), which may be attributed to the direct oxidation of Mn(II) by UV light with wavelengths below 240 nm.[23] The removal of Mn was obviously suppressed with 50 mg L^{-1} superoxide dismutase (SOD), which demonstrated that $O_2^{\bullet-}$ mainly accounted for the oxidation of Mn(II) (Fig. 3a). The presence of $O_2^{\bullet-}$ was further confirmed through electron paramagnetic resonance (EPR)

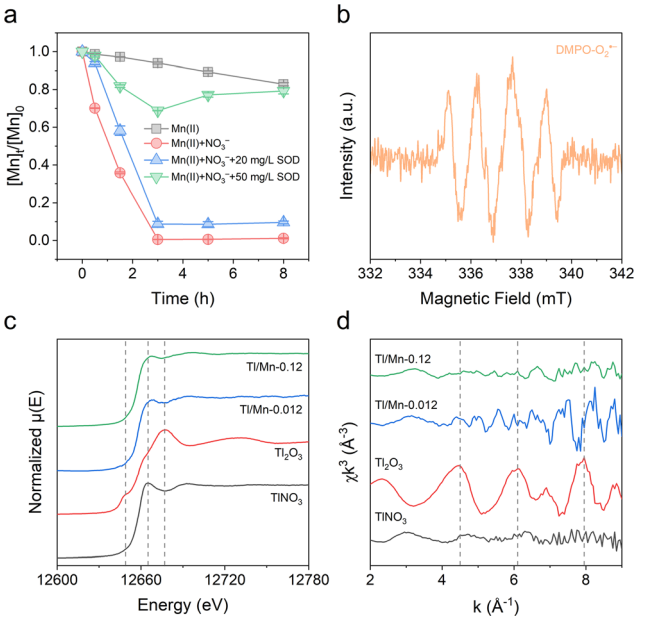

Fig. 3 (a) The effect of SOD on the removal kinetics of Mn. (b) The EPR spectrum of $O_2^{\bullet-}$ trapped by DMPO. Tl L_{III}-edge (c) XANES and (d) k^3-weighted EXAFS spectra of the solid samples collected at 8 h from Tl/Mn-0.012 and Tl/Mn-0.12.

spectroscopy using DMPO as a spin-trapping agent (Fig. 3b). A distinctive absorption peak at 258 nm (Fig. S9, SI), originating from the Mn(III)–pyrophosphate complex, indicated the formation of Mn(III) intermediates.[24] Mn(III) is thermodynamically unstable and can be further converted into Mn(IV) through either disproportionation or oxidation. Recent research has demonstrated that the disproportionation of Mn(III) intermediates is the main pathway for the photochemical generation of Mn(IV) oxide.[25]

δ-MnO_2 is easily transformed by changes in external redox conditions. The concentration of Mn(II) serves as a critical factor governing the structural evolution of δ-MnO_2. At pH 8.0, no change in the phase of δ-MnO_2 was detected when [Mn(II)]/[Mn] ≤ 2%, whereas the transformation to feitknechtite occurred when the ratio reached 10%.[26] In this study, the rapid decline of Mn(II) concentration during the reaction (Fig. 1a) restricted the comproportionation reactions to the initial stage, resulting in the decrease of Mn AOS (Fig. 1c). Moreover, the interaction between δ-MnO_2 and Mn(II) is dependent on pH. Mn(II) only interfered with the stacking of δ-MnO_2 sheets at pH < 7.0, while δ-MnO_2 underwent bulk structural conversion to manganite and hausmannite through a feitknechtite reaction intermediate within the pH range of 7.0–8.5.[20] This transformation process elucidates the coexistence of feitknechtite and hausmannite with δ-MnO_2 in the present study, in contrast to the sole presence of δ-MnO_2 observed in an earlier study where the pH decreased from 8.9 to around 7.0 after 1 h.[5] In addition to Mn(II) concentration and pH, coexisting ions control the transformation of δ-MnO_2.[27] It is well established that metal cations can kinetically hinder the transformation of δ-MnO_2 by competing with Mn(II) for active sites.[28,29] Similarly, the competitive adsorption between Mn(II) and Tl on δ-MnO_2 in this study inhibited its reductive transformation, thereby leading to an increase in the apparent oxidation rate of Mn(II) (Table S1, SI).

The formation and transformation of MnO_x significantly influence the fate and transport of Tl. Tl and Mn showed similar distribution patterns, and the atomic ratios of Tl reached 0.20% and 1.17% in the solid samples collected from Tl/Mn-0.012 and Tl/Mn-0.12 at 8 h, respectively, confirming the effective Tl immobilization by MnO_x (Fig. S10, SI). During the formation of δ-MnO_2, cations (*e.g.*, Mn, Na, Tl) are adsorbed to neutralize the negative charges generated by Mn(IV) vacancies.[30] The fraction of $NH_2OH{\cdot}HCl$-extractable Tl (*i.e.*, more stable Tl species) in *in situ* formed MnO_x was higher than that in *ex situ* MnO_x (Fig. S11, SI), indicating that partial Tl was removed through the coprecipitation process during the nucleation and growth of MnO_x. Notably, unlike transition metals such as Ni(II) and Zn(II), Tl(I) has a significantly different ionic radius from Mn(III) and Mn(IV), making its incorporation into the MnO_x lattice unlikely.[31] The Tl L_{III}-edge X-ray absorption near-edge structure (XANES) spectra indicated that the sorbed Tl was primarily Tl(I) (Fig. 3c), consistent with the XPS results (Fig. S12, SI). Moreover, the corresponding extended X-ray absorption fine structure (EXAFS) spectra showed very low first-shell amplitudes similar to $TlNO_3$ (Fig. 3d). Tl(I) can be oxidized to Tl(III) by the reactive species generated from nitrate photolysis or the vacant octahedral sites of δ-MnO_2.[32] However, the oxidation of Tl(I) was significantly suppressed in the presence of Mn(II), as evidenced by the negligible detection of Tl(III) in both solution (Fig. S13, SI) and MnO_x (Fig. 3c). The standard redox potential of Tl(III)/Tl(I) (E_0 = +1.252 V) is slightly higher than that of Mn(IV)/Mn(II) (E_0 = +1.224 V), indicating a thermodynamic preference for the oxidation of Mn(II) over Tl(I) by reactive oxygen species when they coexist. Furthermore, Mn(II) + Mn(IV) ⇌ 2Mn(III) leads to a reduction in the oxidative capacity of δ-MnO_2 toward Tl(I). Similarly, partial reduction of δ-MnO_2 induced by Fe(II) or HEPES effectively inhibited the oxidative uptake of Tl.[33] In addition, the transformation process of δ-MnO_2 will lead to the repartitioning of Tl due to the distinct affinities of MnO_x with different properties and structures toward Tl. Recent studies have shown that the conversion of δ-MnO_2 to manganite leads to the release of Tl in highly reducing environments (10 mM Mn(II)).[19] Although the reductive transformation of δ-MnO_2 was unfavorable for Tl immobilization (Fig. S14, SI), the concentration of Tl continued to decrease overall (Fig. 1d), which was attributed to the continuous generation of δ-MnO_2 with high sorption capacity.

In conclusion, we revealed the details about the coupling of the light-driven Mn redox cycle with Tl immobilization (Fig. 4). Mn(II) was oxidized to δ-MnO_2 by $O_2^{\bullet-}$ generated during the photolysis of nitrate, while surface-adsorbed Mn(II) facilitated the reductive transformation of δ-MnO_2. Furthermore, photoreduction of the formed MnO_x produced Mn(II) for the next round of oxidation, which facilitated the continuous generation of δ-MnO_2. In the presence of Tl(I), the phase transformation process was suppressed due to the competition between Mn(II) and Tl(I). In addition, the oxidation of Tl(I) was inhibited by

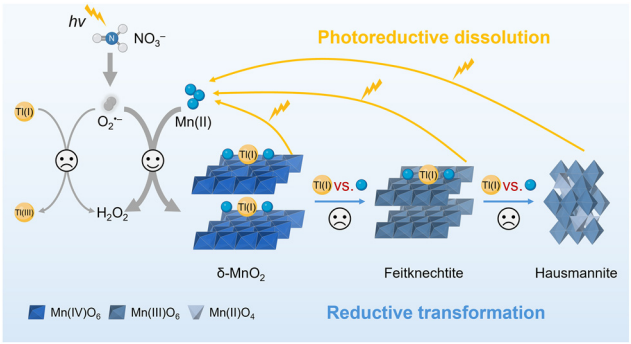

Fig. 4 Schematic for the coupling of the Mn redox cycle with Tl immobilization.

Mn(II), and Tl(I) was effectively removed through adsorption and coprecipitation during the formation of MnO_x. The concentrations of Mn and nitrate, as well as the Tl/Mn molar ratio employed in this study, are environmentally relevant.[33–35] Notably, the coupled effect of Mn(II) oxidative crystallization and Tl immobilization was also observed under natural solar irradiation, albeit proceeding at a slower rate compared to laboratory experiments (Fig. S15, SI). This study validates the crucial role of light in driving Mn redox cycling, particularly in environments unfavorable for microorganisms (*e.g.*, extreme temperatures, strong acidity/alkalinity). This enhances our understanding of MnO_x phase evolution in the environmental Mn cycle, explaining their diversity in nature. Furthermore, Mn redox cycling is often coupled with elemental cycles and organic matter degradation. To the best of our knowledge, this study is the first to uncover the complex photochemical interactions between Mn and Tl. The UV/NO_3^- technology demonstrated here presents a practical pathway for treating industrial wastewater containing Mn and other metal contaminants, enabling their simultaneous removal and facilitating efficient metal recovery and utilization.

This study was financially supported by the National Natural Science Foundation of China (42272045 and 42225203), Natural Science Foundation for Distinguished Young Scientists of Guangdong Province (2023B1515020006), Science and Technology Planning Project of Guangdong Province (2024B0303390002 and 2023B1212060048), and the Basic and Applied Basic Research Foundation of Guangdong Province (2023A1515110854). This is contribution No. IS-3734 from GIGCAS.

Conflicts of interest

There are no conflicts to declare.

Data availability

The data supporting this article have been included as part of the supplementary information (SI). Supplementary information includes experimental details, additional figures, and supporting tables. See DOI: https://doi.org/10.1039/d5cc05797c.

Notes and references

1 J. E. Post, *Proc. Natl. Acad. Sci. U. S. A.*, 1999, **96**, 3447–3454.
2 J. Liu, Q. Chen, Y. Yang, H. Wei, M. Laipan, R. Zhu, H. He and M. F. Hochella, *Earth-Sci. Rev.*, 2022, **232**, 104105.
3 B. M. Tebo, J. R. Bargar, B. G. Clement, G. J. Dick, K. J. Murray, D. Parker, R. Verity and S. M. Webb, *Annu. Rev. Earth Planet. Sci.*, 2004, **32**, 287–328.
4 T. G. Spiro, J. R. Bargar, G. Sposito and B. M. Tebo, *Acc. Chem. Res.*, 2010, **43**, 2–9.
5 H. Jung, T. S. Chadha, D. Kim, P. Biswas and Y.-S. Jun, *Chem. Commun.*, 2017, **53**, 4445–4448.
6 H. Jung, X. Xu, B. Wan, Q. Wang, O. J. Borkiewicz, Y. Li, H. Chen, A. Lu and Y. Tang, *Geochim. Cosmochim. Acta*, 2021, **312**, 343–356.
7 Z. Gao, P.-I. Chou, J. Liu, Y. Zhu and Y.-S. Jun, *ACS Nano*, 2022, **16**, 20238–20250.
8 Z. Gao, J. Liu, C. Skurie, Y. Zhu and Y.-S. Jun, *Water Res.*, 2022, **222**, 118831.
9 F. Li, H. Yin, T. Zhu and W. Zhuang, *Eco-Environ. Health*, 2024, **3**, 89–106.
10 I. Szlamkowicz, J. Stanberry, K. Lugo, Z. Murphy, M. Ruiz Garcia, L. Hunley, N. P. Qafoku and V. Anagnostopoulos, *ACS Earth Space Chem.*, 2023, **7**, 1–10.
11 A. L. J. Peter and T. Viraraghavan, *Environ. Int.*, 2005, **31**, 493–501.
12 T. Huang, D. Song, Q. Fang, C. Yang, D. Wu, S. Li, Y. Luo, Y. Yan and Z. Hu, *Chem. Eng. J.*, 2023, **469**, 143751.
13 Y. Huang, Z. Xiao, S. Wu, X. Zhang, J. Wang and X. Huangfu, *Sci. Total Environ.*, 2024, **953**, 176028.
14 Z. M. Migaszewski and A. Gałuszka, *Rev. Environ. Sci. Bio/Technol.*, 2021, **20**, 5–30.
15 H. Xu, Y. Luo, P. Wang, J. Zhu, Z. Yang and Z. Liu, *Water Res.*, 2019, **165**, 114981.
16 F. F. Marafatto, R. Dähn, D. Grolimund, J. Göttlicher and A. Voegelin, *Geochim. Cosmochim. Acta*, 2021, **302**, 193–208.
17 A. Voegelin, N. Pfenninger, J. Petrikis, J. Majzlan, M. Plötze, A.-C. Senn, S. Mangold, R. Steininger and J. Göttlicher, *Environ. Sci. Technol.*, 2015, **49**, 5390–5398.
18 L. Zhang, Y. Yang, X. Xu, H. Xiao, S. Deng, X. Han, F. Xia and Y. Jiang, *Sep. Purif. Technol.*, 2022, **300**, 121821.
19 W. Chen, J. Liu, X. Huangfu, Y. Chen, W. Zhong, Y. Liu, Y. Huang and H. Liu, *Environ. Sci. Technol.*, 2025, **59**, 9221–9234.
20 J. P. Lefkowitz, A. A. Rouff and E. J. Elzinga, *Environ. Sci. Technol.*, 2013, **47**, 10364–10371.
21 F. F. Marafatto, M. L. Strader, J. Gonzalez-Holguera, A. Schwartzberg, B. Gilbert and J. Peña, *Proc. Natl. Acad. Sci. U. S. A.*, 2015, **112**, 4600–4605.
22 G. Luther, *Geomicrobiol. J.*, 2005, **22**, 195–203.
23 A. D. Anbar and H. D. Holland, *Geochim. Cosmochim. Acta*, 1992, **56**, 2595–2603.
24 X. Wang, M. R. Jones, Z. Pan, X. Lu, Y. Deng, M. Zhu and Z. Wang, *Water Res.*, 2024, **263**, 122198.
25 T. Zhang, L. Liu, W. Tan, S. L. Suib and G. Qiu, *Chemosphere*, 2021, **262**, 128082.
26 H. Zhao, M. Zhu, W. Li, E. J. Elzinga, M. Villalobos, F. Liu, J. Zhang, X. Feng and D. L. Sparks, *Environ. Sci. Technol.*, 2016, **50**, 1750–1758.
27 M. Shi, Q. Li, Q. Wang, X. Yan, B. Li, L. Feng, C. Wu, R. Qiu, H. Zhang, Z. Yang, W. Yang, Q. Liao and L. Chai, *J. Environ. Sci.*, 2024, **139**, 496–515.
28 Q. Wang, P. Yang and M. Zhu, *Geochim. Cosmochim. Acta*, 2019, **250**, 292–310.
29 P. Yang, K. Wen, K. A. Beyer, W. Xu and M. Zhu, *Geochim. Cosmochim. Acta*, 2025, **393**, 155–169.
30 J. Aguilar-Carrillo, L. Herrera-García, I. A. Reyes-Domínguez and E. J. Gutiérrez, *Environ. Pollut.*, 2020, **257**, 113492.
31 K. D. Kwon, K. Refson and G. Sposito, *Geochim. Cosmochim. Acta*, 2013, **101**, 222–232.
32 C. L. Peacock and E. M. Moon, *Geochim. Cosmochim. Acta*, 2012, **84**, 297–313.
33 S. Wick, J. Peña and A. Voegelin, *Environ. Sci. Technol.*, 2019, **53**, 13168–13178.
34 Z. Gao, C. Skurie and Y.-S. Jun, *Environ. Sci.: Nano*, 2022, **9**, 3756–3765.
35 Z. Gao, G. Y. Jung, P.-I. Chou, O. J. Borkiewicz, M. Newville, R. Mishra and Y.-S. Jun, *Environ. Sci. Technol.*, 2025, **59**, 10455–10466.